Microscopic origin of light scattering in tissue

Alois K. Popp, Megan T. Valentine, Peter D. Kaplan, and David A. Weitz

A newly designed instrument, the static light-scattering (SLS) microscope, which combines light microscopy with SLS, enables us to characterize local light-scattering patterns of thin tissue sections. Each measurement is performed with an illumination beam of 70-μm diameter. On these length scales, tissue is not homogeneous. Both structural ordering and small heterogeneities contribute to the scattering signal. Raw SLS data consist of a two-dimensional intensity distribution map $I(\theta, \varphi)$, showing the dependence of the scattered intensity I on the scattering angle θ and the azimuthal angle φ. In contrast to the majority of experiments and to simulations that consider only the scattering angle, we additionally perform an analysis of the azimuthal dependence $I(\varphi)$. We estimate different contributions to the azimuthal scattering variation and show that a significant fraction of the azimuthal amplitude is the result of tissue structure. As a demonstration of the importance of the structure-dependent part of the azimuthal signal, we show that this function of the scattered light alone can be used to classify tissue types with surprisingly high specificity and sensitivity.

OCIS codes: 170.6480, 170.4730, 180.0180.

1. Introduction

The search for noninvasive medical techniques leads naturally to the use of light. A growing number of optical-medical applications such as photodynamic therapy, laser-based microsurgery, optical-coherence tomography,[1] and diffuse-optical tomography[2,3] are based on light–tissue interactions, and thus ultimately on the single-scattering event. Our understanding of the single-scattering event in tissue is limited. Although a complete spatial map of the complex index of refraction is sufficient to calculate it with Maxwell's equations,[4,5] exact calculations are computationally tedious and require an impractical level of detail, especially knowledge of both cellular contents and exact arrangements of scattering objects. We show that by analyzing light-scattering data along two angular axes, we can partially account for both tissue contents and their organization.

Because most medical techniques have been developed for bulk tissue, many experimental approaches and their analytical or numerical support rely on average tissue-scattering properties. These are expressed as scattering and absorption coefficients[6–9] that are calculated from raw data under the assumption of a multiple scattering model. These average scattering properties have been sufficient input to models based on the diffusion approximation, transport theory, and Monte Carlo techniques to support the remarkable progress in developing optical tomographic techniques in recent years.[3,10–12] None of these efforts considers cellular length scales.[10,13–16] Because tissue is heterogenous on length scales between 1 and 1000 μm, attempts to use continuum light-transport models on shorter-length scales may not succeed.

Unlike diffuse-optical tomography, some optical diagnostic techniques are sensitive to cellular length scales.[17–19] Pathologists, for example, see the earliest signs of disease by microscopic examination of structures. The hunt for a light-scattering signature of pathological microstructure has motivated studies of tissue model systems. These studies of tissues and cell suspensions focused on measurements of $I(\theta)$, known as the phase function or form factor.[20–22] Most of these investigations have been performed in backscattering geometry to mimic *in vivo* measurements.[22–24] The form factor can be calculated for scatterers of various sizes and shapes. It is natural, therefore, that static light-scattering (SLS) models have focused on the content rather than on the structure of tissue. However, it is not possible to look at tissue micrographs without noting the

---

When this research was performed, A. K. Popp, M. T. Valentine, and D. A. Weitz were with the Department of Physics and the Division of Engineering and Applied Sciences, Harvard University, Cambridge, Massachusetts 02138. A. K. Popp (Alois.Popp@unilever.com) is now with the Unilever Res. NL, 3133 AT Vlaardingen, The Netherlands. P. D. Kaplan is with Unilever Research U.S., Edgewater, New Jersey 07020.

Received 7 October 2002; revised manuscript received 19 December 2002.
0003-6935/03/162871-10$15.00/0

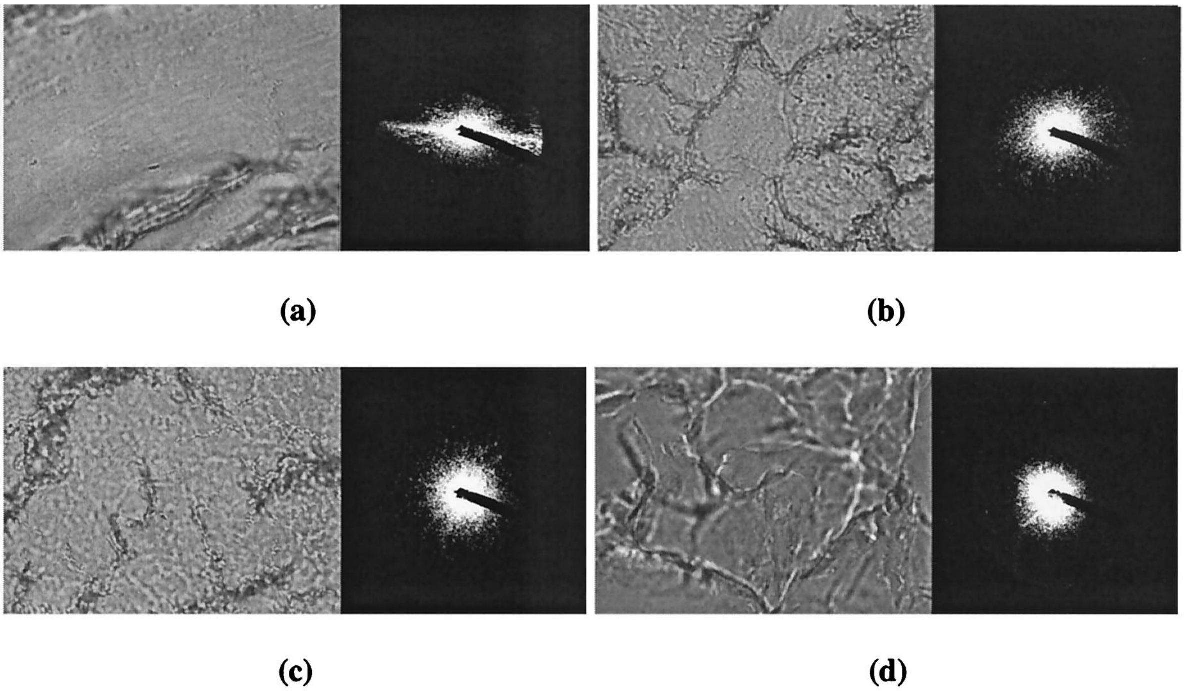

Fig. 1. Real-space images (left) and scattering patterns (right) from different tissues. The real-space images show a field of view of 60-μm width, displaying the surface onto which the incident laser beam is directed. The scattering patterns are intensity distributions and show bright spots for high scattered intensity. In (a) *Rana* Sartorius muscle fibers are oriented parallel to the surface of the coverslip ("striated muscle ‖"). Influence of orientation of the fibers on image and scattering patterns can be observed by a comparison with (b), a striated muscle sample mostly cross-sectionally oriented to the surface of the coverslip ("striated muscle ⊥"). (c) and (d) Real-space images and scattering patterns from lung smooth muscle and skin (stratum corneum), respectively. In skin, the amount of light scattered on the left-hand side of the beam block is much higher than the intensity on the other side, another manifestation of anisotropy. The smooth muscle scatters light more isotropically.

complex spatial arrangement of different cell types, organelles, and extracellular matrix. That the organization itself must contribute to light scattering is well known implicitly. For example, polarized light microscopy, a useful tool for pathologists, is sensitive to birefringence, which is a consequence of structural alignment in tissue. Light-scattering techniques have two general advantages over direct imaging that may lead to their preferred use in some biomedical applications. First, light scattering captures data of direct relevance to light transport. Second, the interpretive strategies are more naturally quantitative than approaches based on image analysis. Since both light scattering and microscopy are sensitive to index-of-refraction contrast, they both should be able to detect local optical property changes in tissue owing to differences in microstructure. The development of useful light-scattering approaches could lead to both theoretical advances and practical applications in automated tissue diagnosis.

To study the role of organization at the cellular scale in light–tissue interactions, we have developed a technique that combines SLS with microscopy. The combination will guide our interpretation of scattering from heterogeneous samples. The light-scattering apparatus is built into a fully functional microscope, which provides simultaneous bright-field images and two-dimensional light-scattering patterns.[25,26] We have collected scattering patterns from several tissues. In addition to reproducing previously published form factor results, these data point to the importance of organization as seen by both a power-law analysis of the form factor and by analyzing the azimuthal scattering patterns for between-tissue differences. After looking at the total azimuthally scattered power, we construct a reduced-space version of the Fourier representation of the azimuthal scattering patterns. The statistics of the patterns in this representation show diagnostic promise and point to future applications in biomedical optics.

Because the data that follow are qualitatively different from those of other techniques, we briefly preview both bright-field images and scattering patterns of different tissue types. In Fig. 1(a), a striated muscle has been mounted with fibers aligned parallel to the cover slip (striated ‖); the same type of muscle with fibers aligned cross sectionally to the cover slip is shown in Fig. 1(b). Muscle is composed of elongated fibers, which are oriented in striated muscle and globally disoriented in the lung smooth muscle shown in Fig. 1(c). Skin, Fig. 1(d), is a heterogeneous tissue containing large structures such as hairs and sweat ducts. The influence of different organizational properties on SLS patterns is displayed in the scattering patterns, which demonstrate that directional ordering contributes to anisotropic scattering patterns. Each example has some degree of ordering: The periodic organization of parallel

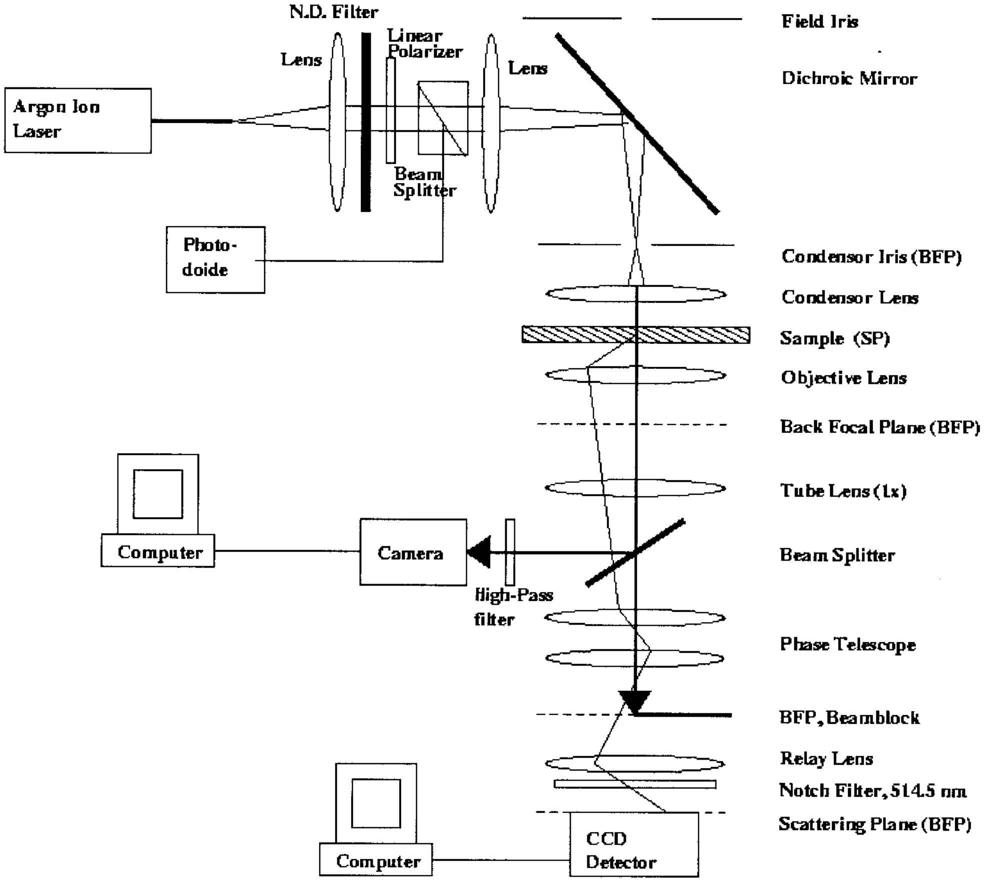

Fig. 2. Schematic of the SLS microscope. A laser beam from an Ar^+-ion laser (Coherent Innova 304, 514.5 nm), attenuated to typically 50 μW, is coupled into the illumination path of a commercially available inverted microscope (Leica DM-IRBE). A photodiode monitors the incoming beam intensity, which allows us to correct for differences in input intensity. The laser beam is collimated at the sample plane to a beam diameter of 70 μm. The conventional objective lens of the microscope (plan-apochromatic, 100× magnification) collects both forward-scattered and transmitted light. Pixelized scattered-light intensity distributions are measured at a 16-bit cooled CCD detector (Princeton Instruments, Model CCD-512SF, 512 × 512 array of 24-μm-sized square pixels) located on an extension of the microscope. The scattering patterns on the detector are enlarged images of the back focal plane of the objective (BFPO), with the transmitted beam blocked. In addition, the same regions of our samples are imaged by means of conventional bright-field microscopy by diverting a portion of the illuminating light to the side camera port equipped with a video camera.

aligned muscle fibers results in highly structured azimuthal spikes [Fig. 1(a)]. The scattering from the perpendicularly oriented striated muscle is isotropic [Fig. 1(b)] suggesting that there is little order in the plane perpendicular to the muscle's contractile axis. The sarcomeres in lung smooth muscle [Fig. 1(c)] have local order that is difficult to detect in the bright-field image but results in small scattering anisotropies. Rough surfaces and interfaces such as those found on the top layer of skin, the *stratum corneum*, cause vague directionality, and sharp boundaries result in spikes or lines in the scattering patterns [Fig. 1(d)]. The scattering patterns of these four images quantitatively reflect the qualitative features observed in the images.

2. Materials and Methods

2.A. Sample Processing

We have studied four different tissue types: porcine smooth muscle, striated muscle, and skin, as well as *Rana bifida* Sartorius muscle. Porcine tissues for this study were collected from a single animal. The samples were frozen in liquid nitrogen immediately after collection and cut into 20-μm-thick slices by use of a standard cryomicrotome. The slices were directly transferred from the knife to a small coverslip (18 mm × 18 mm), which was mounted on a microslide, with ultravacuum grease to seal the chamber. The slides were stored for up to 2 weeks at −20 °C or at 4 °C for less than 24 h prior to measurement.

2.B. Static Light-Scattering Microscope

The physical principles as well as instrumental details of the SLS microscope (Fig. 2) have been described elsewhere in detail.[25–27] Briefly, a laser beam is coupled into the illumination path of an inverted microscope. In the sample plane, the beam is collimated with a diameter of 70 μm. Scattered light, collected by the objective lens, forms a scattering pattern in the back focal plane. This pattern is reimaged onto an intermediate plane containing a beam block to remove the transmitted beam and finally is relayed onto a cooled CCD detector. This detector has 16-bit dynamic range with a 512×512 array of 24 μm^2 pixels. Before a quantitative investigation of the scattering function is possible, all scattering patterns are divided by the exposure time and the input intensity and corrected for small effects including pixel differences and flare at low angles,[25] thus reducing the influence of measurement errors to typically below 1%. Flare or stray light is measured by scattering from an empty sample chamber.

The corrected intensity distribution on the detector is converted into the scattering function $I(\theta, \varphi)$ on the basis of considerations of optics and scattering geometry. The scattering angle θ of a beam scattered by a sample of refractive index n_S is a function of the radial distance to the transmitted beam on the detector, δx. This relationship is calibrated by measurement of the pixel position of diffraction peaks caused by scattering from a graticule of index of refraction n_G. Using Bragg's law to relate scattering angles to the position of diffraction peaks on the detector δx and Snell's law to take account of various indices of refraction, we obtain a calibration curve with a calibration constant, C.

$$\theta = \left[\arcsin\left(\frac{n_G}{n_S} C \delta x \right) \right]. \tag{1}$$

Simultaneous bright-field imaging is performed with a CCD video camera attached to the side port of the microscope.

We average over the azimuthal angle φ by dividing the pattern into concentric rings around the unscattered beam to obtain the form factor $I(\theta)$. To obtain $I(\varphi)$, we average over θ by binning the image into 360 wedges of 1°. For sufficiently sampling the variations of our tissue, experiments were performed for each thin section at 25–35 randomly selected fields of view.

The analysis below mainly concerns the light-scattering patterns. The images are used implicitly to ensure that patterns come from the tissue of interest. The scattering pattern and the image are not merely different representations of each other. Real-space and Fourier-space results are not connected by a simple transformation, because of the different optical properties of the light sources. The coherent laser illumination in the scattering measurement has a large effective depth of field and truly probes three-dimensional volume.[25] The imaging modality does depend on all three dimensions but is carefully designed to present planar images.

3. Results

We begin by comparing our results with previously published data. Typically, scattering patterns are analyzed with respect to the scattering angle θ and compared with the Henyey–Greenstein function, an empirical approximation for Mie scattering from particles with a distribution of sizes[20,28]

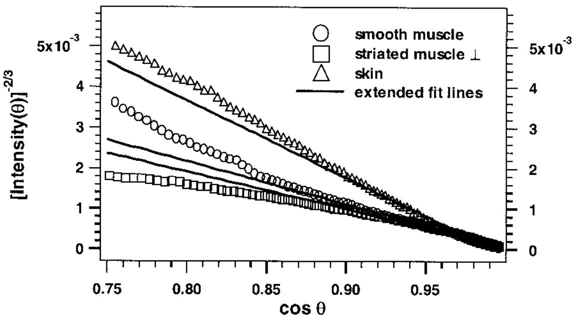

Fig. 3. Henyey–Greenstein fits of the form factors $\langle I(\theta) \rangle_\varphi$ for the interval $0.995 \geq \cos\theta \geq 0.9$, with the method of Jacques *et al.*[20] The systematic deviations from the small-angle Henyey–Greenstein parameters at larger angles are matched by previous studies. These data show the compatibility of averages of our measurements to bulk measurements that inherently average over a large illumination area.

$$I(\theta) = I_0 \frac{1 - g_{\mathrm{HG}}^2}{(1 + g_{\mathrm{HG}}^2 - 2 g_{\mathrm{HG}} \cos\theta)^{3/2}}. \tag{2}$$

We have extracted the scattering-angle-dependent signal $I_{ij}(\theta)$ of each local scattering pattern i and averaged over the ensemble of fields of view for each tissue j. In Fig. 3 we display both the average form factors $\langle I_j(\theta) \rangle = \sum_{i=1}^{n} I_{ij}(\theta)/n$ for each tissue type and fits to the Henyey–Greenstein function. The Henyey–Greenstein phase function [Eq. (2)] contains no absolute cross section and only one parameter, the anisotropy g_{HG}, a measure of forward-scattering probability. In the Rayleigh-scattering limit of particles much smaller than the illumination wavelength, g_{HG} approaches zero, whereas the sharp forward scattering cone of large particles is described by a g_{HG} close to 1. The axes and range of angles in Fig. 3 are chosen to match the convention of Jacques *et al.*[20] Both the quality of the fits and the value of g_{HG} are in agreement with their results for thin tissue sections (Table 1). In general, the match between the Henyey–Greenstein function and light-scattering data from thin tissue sections is poor at large angles,[18] and only a correction to higher-order terms is able to produce better agreement.[29,30]

As an approximation of Mie scattering, the Henyey–Greenstein function neglects the interference resulting from organized tissue structure. If we took a different point of view, that tissue organization is the dominant factor in light–tissue interactions, then we would adopt a model based on the statistics of scattering from aggregates.[31] Aggregate scattering models lead to power-law scattering functions[32] that can be used to describe aggregation of bacterial cells. Power-law functions are known to connect the theoretical framework for phase transitions to experimental systems. Experimentally determined power-law coefficients are often used as input to the theory of gelation processes of polymers

Table 1. Average Tissue-Scattering Properties[a]

	Skin	Smooth Muscle	Striated Muscle $\perp$	Striated Muscle $\parallel$
Asymmetric anisotropy	0.48 ± 0.18 (0.47)	0.27 ± 0.15 (0.22)	0.24 ± 0.1 (0.20)	0.46 ± 0.18 (0.41)
Random scattering component	0.48 ± 0.16 (0.43)	0.65 ± 0.13 (0.68)	0.68 ± 0.09 (0.67)	0.36 ± 0.15 (0.34)
Power-law coefficient z	3.63 ± 0.03	2.37 ± 0.01	2.62 ± 0.02	2.67 ± 0.04
Anisotropy factor g_{HG}	0.872	0.907	0.879	0.869

[a] Major azimuthal scattering components, power-law coefficients and Henyey–Greenstein factors g_{HG}. The asymmetric anisotropic scattering signal can be used to quantify differences in structural ordering between tissues. Moreover, the structure-independent scattering fraction is given. It consists of the isotropic amplitude and the part of the symmetric amplitude, which is linked to scatterer size. This component highlights the difference between the less-ordered tissues and the symmetrically aligned muscle fibers of the striated muscle $\parallel$ sample (Figs. 6 and 7). Here average values are shown with standard deviations and medians in parentheses. Porcine skin is different from muscle in that its power-law coefficient is between 3 and 4, whereas the other samples show coefficients between 2 and 3.

and colloids.[33] To match the notation of these models, we change axes from $I(\theta)$ to $I(q)$. The wave vector $q = 4\pi n_S \sin(\theta/2)/\lambda$ is a function of the scattering angle θ, the laser wavelength λ, and the refractive index of the sample n_S. We show in Fig. 4 that a power-law decay, $I(q) \sim q^{-2}$, does describe our data well. Light scattering from many systems, such as gels and colloidal aggregates, is described by a power law. In these systems, the power law results from interference between neighboring particles in an aggregate and can be derived mathematically with simple geometric relationships and an integral over the pair correlation function.[34] The power-law coefficient z is a measure of the structures' dimensionality.[35] Recently, it has been stated that this concept is applicable to tissue as well.[4,36,37] Bulk structures of dimension d have decay coefficients $z = d$ up to 3, with scatterers organized within the surface of an object thicker than $1/q$ scatter light with a power law that decays with $z = 6 - d$ between 3 and 6. The best-fit values of z to the form factors in Fig. 4 are shown in Table 1. Skin appears to be organized differently than the other tissues. Whereas all non-skin samples have decay coefficients between 2.3 and 2.7, the decay coefficient for skin is 3.6. Within the framework of fractal geometry, we can explain this difference by arguing that scatterers in skin are organized along a macroscopic surface, whereas muscle scatters light from fibrous particles imbedded throughout the bulk of the tissue, even though we have sampled only a thin slice of that bulk-organized tissue. Thus the plate-like cells of the *stratum corneum* have scattering properties distinct from other tissues. For the fractal dimensions d, we obtained values between 2.3 and 2.7. These values are in accordance with results of a previous study[36] ($d = 2.6 - 2.72$) on a number of tissues that are different from ours. There, the fractal dimension has been calculated from Fourier-transformed microscope images of different resolution. In summary, although our angular scattering data match previously published results, a power-law analysis supports the concept that the arrangement of scattering objects contributes qualitatively to light scattering in tissue.

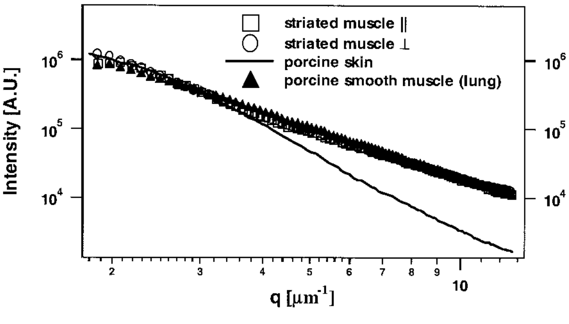

Fig. 4. Slice-averaged form factors of different tissue types show a power-law decay $I(q) \sim q^{-z}$. The decay law for skin ($z = 3.6$) is substantially different than for the other tissue types ($z \approx 2.5$).

The novelty of our data is the inclusion of azimuthal resolution (Fig. 5). There exist excellent literature about azimuthal variation in the intensity of light backscattered from bulk tissue and tissue phantoms, in which underlying polarization effects are described as well.[23,24] Our experiment is different in experimental design and investigated systems, as we examine the azimuthal variation in forward scattering from thin tissue slices. We observe a significant amount of light scattered into complex azimuthal patterns (Fig. 4). In the following, we argue that both contents and structural organization contribute to these patterns. In general, not all the azimuthally varying signal can be assumed to be the signature of organization, and a more detailed analysis is needed to separate contributions of different effects. We now test the importance of azimuthal scattering in two steps: First, we quantify the different contributions to show that a significant part of the light–tissue interaction is due to structure. Second, we develop a scheme that might be useful for identifying tissue types solely on the basis azimuthal scattering.

To separate the effects of particle shape from organization, which both contribute to anisotropy in scattering, symmetry analysis of the single amplitudes is crucial. In general, the polarization-dependent single scattering amplitude $\mathbf{E}'$ in relation to the incident beam $\mathbf{E}$ can be described by the 2×2 scattering matrix $\mathbf{S}$ for any object.[36] Because the intensity is equal to the square of the field, the scattered intensity matrix contains 4×4 elements. This matrix is easily transformed into the 4×4 sized Mueller matrix that completely describes the polarization state

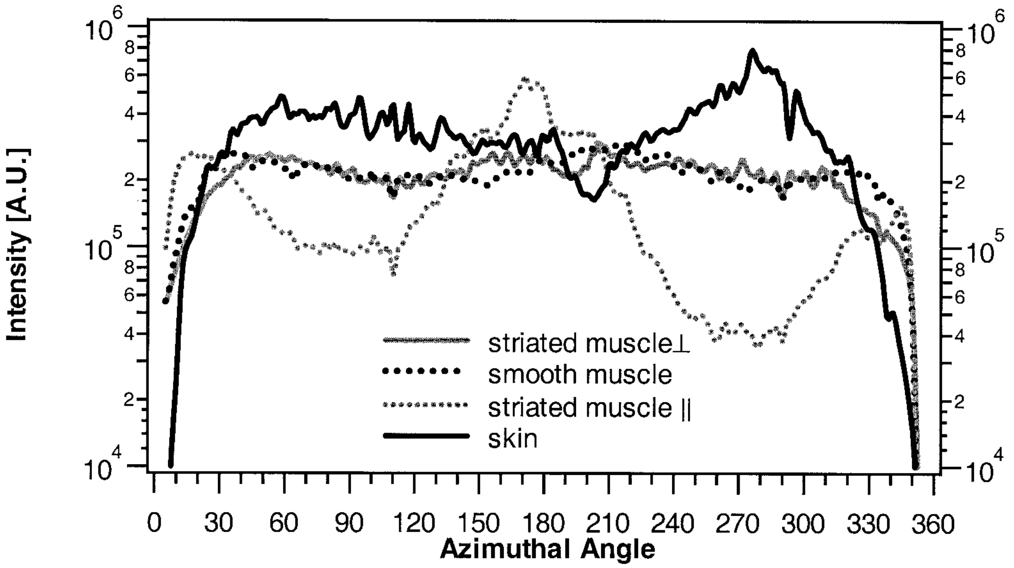

Fig. 5. Radial intensity distribution $I(\varphi)$ of a single measurement for each investigated tissue type. The skin sample, as well as the parallel oriented muscle sample, shows a large amount of scattering dependent on the azimuthal angle. Samples showing unordered structures have by far less anisotropic scattering.

of scattered light.[37] For a sample of homogenously distributed approximately spherical particles such as nuclei, which is the usual assumption when considering light–tissue interactions, the azimuthal signal can be described with application of Mie theory.[36] In this case, a linearly polarized incident laser beam leads to an azimuthal signal of 180° symmetry. Details of the pattern such as scattering intensities depend on the state of polarization of the input beam and on the size of the scatterer. A successful and growing literature of measurements taken in backscattering geometry is based on this scheme.[22–24] In these experiments, bulk tissues and tissue phantoms produce characteristic arrays of Mueller matrices in which the 4×4 array is presented as an array of images and each point on the sample contributes a pixel to each image.

Since the Mie-scattering pattern is more complex in the backscattering than in the forward-scattering directions, the complexity of patterns observed in these Mueller matrices in diffuse backscattering techniques is higher than that of our forward-scattering data.[23,24,37]

On the other hand, the presence of asymmetric components in experimental data would demonstrate the influence of local differences in particle distribution. These microscopic differences are the building blocks of tissue structure. For effectively estimating the relative importance of this contribution to the light–tissue interaction, we have expanded the experimental data into a Fourier series with complex coefficients c_m:

$$I(\varphi) = \sum_{m=-\infty}^{\infty} c_m \exp(-im\varphi). \tag{3}$$

The real amplitudes $|c_m|$ are independent of the orientation of the sample. To decrease the systematic effects introduced by our beam block, we replace the covered region of typically 10° with data from its 180° symmetric counterpart, since these components are a reasonable zero-order prediction for the total intensity in this small region, leading to a conservative estimate for the asymmetric anisotropy. By back transformation, we ensure that the resulting series represents the original function up to average differences of less than 1%. Using the Fourier coefficients c_m, we can divide the total scattered intensity into a symmetric component $m = 2k$, an asymmetric component $m = 2k + 1$, and an isotropic component $m = 0$. Symmetric and asymmetric components together present the anisotropic intensity.

First, we investigate the asymmetrically scattered light. Its fraction ϵ is

$$\epsilon = \frac{\sum\limits_{m \neq 2k} |c_m|}{\sum\limits_{m=-\infty,\,\infty} |c_m|}, \qquad k \geq 0. \tag{4}$$

In a disordered sample, randomly aligned scatterers will tend to result in $\epsilon = 0$. To avoid overstating the asymmetric anisotropy factor, we calculate ϵ with an upper limit of $m = 10$ instead of ∞. This arbitrary cutoff leads to a conservative estimate that treats high frequencies as if they are part of the isotropic signal.

Across the investigated tissues we see that a significant fraction of scattered light, generally over 20%, scatters asymmetrically (Table 1). This suggests that asymmetric scattering is a significant part of the light–tissue interaction.

In addition, a smaller but not negligible part of the tissue structure itself might be of symmetric shape and would thus contribute to the symmetric amplitude. Prominent examples for symmetric tissue or-

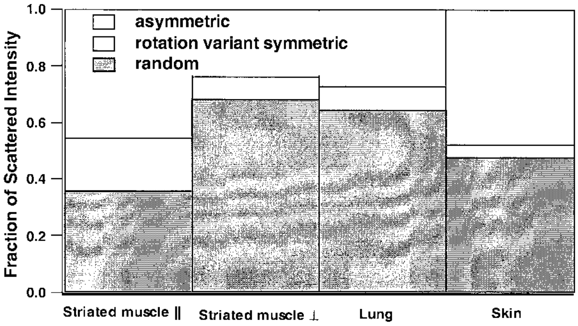

Fig. 6. Composition of azimuthal light scattering of the investigated tissues. Skin (*stratum corneum*) shows the highest asymmetric scattering component of all investigated tissues; striated muscle and lung, the lowest. Up to 50% of the scattered light is scattered asymmetrically. The rest is symmetric or static scattering owing to a random distribution of scatterers ("random"). All investigated tissues suggest that amounts of more than 30% of the scattering are not due to a homogenous distribution of particles. Parallel-aligned striated muscle has the highest rotation-variant symmetric scattering amplitude; skin (*stratum corneum*), the lowest.

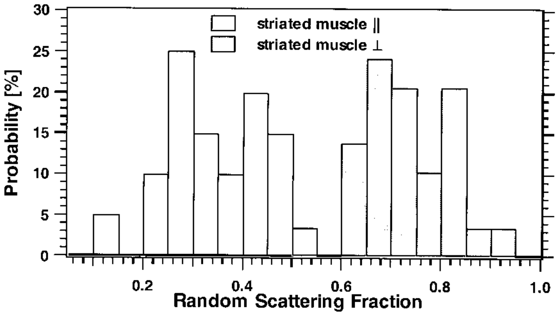

Fig. 7. Distribution of random anisotropic scattering for the two tissue types separable best according to the scattering component that is due to random scatterer distribution. The probability of obtaining a certain "random" scattering fraction is shown versus the fraction itself.

ganization are aligned fibrous structures such as muscle fibers. To identify the structure-dependent symmetric signal, we have resorted to an experimental method. After taking a single measurement, we rotated the sample by at least 90° around the center of the incident beam. Then a second measurement of this spot was taken, and differences in the angular intensity of the symmetric signal were estimated. The scattering signal of a homogenous particle distribution is practically rotation invariant, whereas the rotation of symmetrically aligned fibers leads to the rotation of the related scattering signal. For a rough check of the presence of this effect, distinguishable symmetric peak structures were replaced with the same angular range of the rotated pattern. The resulting pattern was compared with the original pattern. If the symmetric peak structures were due only to a homogenous scatterer distribution, no change in the patterns would be observed. In fact, differences of up to 65% were estimated in single measurements of aligned muscle. This method was extended to all tissue types: First, the amount of anisotropic scattering was quantified with Eq. (4). Then rotated and unrotated patterns were compared by calculation of the minimum of the two intensities for each angle. The resulting component contains the isotropic and the symmetric rotation-invariant scattering signals, both effects of random scatterer distribution. Knowing two of the three contributions, we calculate the remaining intensity needed to reconstruct the original signal. This final component is the rotation-variant symmetric signal that results from symmetric alignment of scatterers. In general, our estimates show that across all tissues a significant fraction of the scattering signal cannot be explained by the assumption of homogenous scatterer distribution in tissues (Table 1). In Fig. 6 we display the sample-averaged contributions to the azimuthal scattering signal for the investigated tissues. Asymmetric and rotation-variant symmetric scattering together present the signal resulting from the presence of irregularly shaped particles and tissue organization. Striated muscle $\|$ shows the strongest influence of asymmetric and symmetric rotation-variant scattering, 45% (Table 1) and 20%, respectively. On average, 65% of the azimuthal signal is due to contributions that together represent tissue organization. The highest fraction of asymmetric scattering, 48% (Table 1), is found in the *stratum corneum* data, which additionally has the lowest fraction of rotation-variant signal and thus the smallest amount of symmetric alignment. Perpendicularly oriented striated muscle has the lowest amount of structure-dependent signal. But since even in this case tissue organization contributes ~35% to the total signal (Table 1), we can assume that tissue structure and organization significantly influence the optical properties of tissues on microscopic length scales.

Tissues are not, in general, homogenous at the cellular scale. Inhomogeneous and irregular tissues present a challenge for pathological tissue typing, though extremely different tissues should separate rather easily. To highlight the differences between tissues, we display distributions of the rotation-invariant symmetric scattering coefficient for the two tissue types that are most different, smooth muscle and striated muscle $\|$ (Table 1) in Fig. 7. Because these distributions only slightly overlap, one might hope that only one parameter alone could be used for tissue typing. Although this is true for extremely different tissues, more subtle differences will require a closer look. As an initial attempt to apply anisotropic scattering to tissue typing, we use the simplest multivariate method, principal component analysis (PCA), to analyze the Fourier coefficients.[39,40] Our goal is to demonstrate that, similar to $I(\theta)$, a high amount of physiologically relevant information is contained in $I(\varphi)$.

The first step in PCA is to organize the data into a $k \times m$ array, where k is the total number of patterns and m is the number of Fourier coefficients. To min-

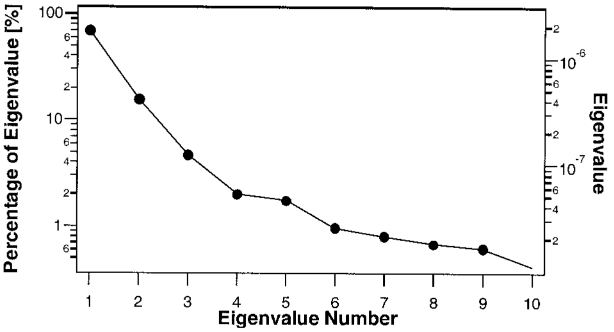

Fig. 8. Eigenvalues of the PCA (right-hand axis) represent the variation of scores of the PCA analysis, performed for all tissues together. They show the pronounced importance of the first four components and can be scaled as percentage of variation (left-hand axis). The figure shows that more than 90% of the variation of the data is represented by the first four principal components.

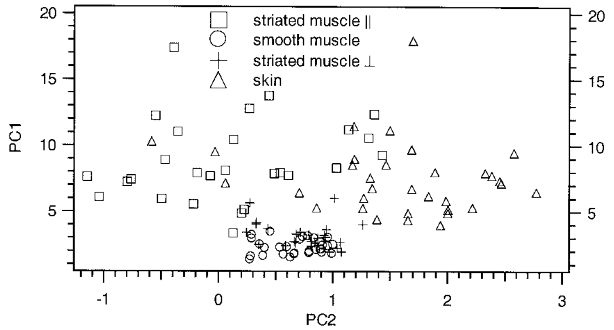

Fig. 9. Scatter plot of PC1 versus PC2: This plot shows the comparably strong variation in principal components of the ordered structures. Much smaller variation is observed for principal components of cross-sectionally oriented striated muscle and of lung smooth muscle, which have no directional order.

imize sampling errors, we reduce our representation from the 360 data points in $I(\varphi)$ to $m = 50$ Fourier amplitudes. Each of the four tissues contributed 25 patterns to our total set of $k = 100$ patterns. Each scattering pattern is represented by m Fourier amplitudes and can be thought of as one point in an m-dimensional data space. This space is vastly larger than the nature of the data requires and is therefore sparsely populated. To find a simple representation of the space of scattering patterns, we diagonalize the matrix and rotate it so that the axes (eigenvectors) are sorted from most to least significant according to the magnitude of their eigenvalues. The eigenvalue spectrum (Fig. 8) indicates that over 90% of the variation can be attributed to the first four principal components. The details of the eigenvectors are somewhat arbitrary and should not be overinterpreted. By keeping only the dimensions along which there is the most variation, we use PCA as a tool for data reduction. More-sophisticated multivariate analysis techniques segment data with greater precision and produce more meaningful axes. We consider the projection of the scattering patterns along the first five principal components to be a "fingerprint." To show how useful this representation is, we present a scatter plot of the projection of the patterns against the first two principal components of all experiments in Fig. 9. This plot highlights the heterogeneity within and between tissues. The two tissue types showing repetitive micrometer-sized structures exhibit large variation in these components, whereas the disordered striated muscle tissue and the lung smooth muscle cluster together tightly, with the exception of a few outliers. For qualitative use of these fingerprints, we apply k-means cluster analysis, a qualitative measure of similarity and difference between multidimensional data. Although this effort is mainly demonstrative, we show that cluster analysis is a useful way to separate the azimuthal light-scattering signature of differently structured homogeneous tissues. The data of striated muscles, skin, and lung smooth muscle are grouped into clusters with a routine packaged with our data-analysis software (IDL, Research Systems Incorporated, Boulder, Colorado, USA). This routine divides the data into clusters with maximal distance between their centers. Since k-means clustering involves an optimization algorithm whose output might be sensitive to initial guesses or might experience local minimum convergence, we checked the algorithm shortly for its robustness by slightly varying the input data, its order, and the number of clusters. Finding no substantial sensitivity to slight variations, we set the number of clusters equal to the actual number of tissue types. The clustering algorithm's output (Table 2) shows the assignment of each field of view to the clusters A, B, C, and X. The distinction between ordered and disordered struc-

Table 2. Results of the Cluster Analysis[a]

Classification	Striated Muscle ∥	Striated Muscle ⊥	Smooth Muscle	Skin	Specificity [%]
A	16	0	0	14	53
B	6	2	0	18	69
C	1	26	28	0	50
X	4	0	2	1	—
Sensitivity [%]	59	93	93	55	

[a] Anisotropy-based classification of tissue by cluster analysis of the scattering patterns along the dimensions of their most significant principal components. Ordered samples (striated muscle ∥, skin) and disordered samples (striated muscle ⊥, smooth muscle) are almost completely separated into different clusters. Sensitivity,[38] the probability for measurements of one tissue type being grouped solely into one cluster, is very high for the disordered muscles.

tures is quite clear: Cluster C contains only disordered structures. Between the two disordered structures, however, no distinction is found by cluster analysis. It is not surprising that we are unable to distinguish cross-sectionally oriented striated from smooth muscle, because as in some fields of view the smooth muscle is a very similar tissue and is locally ordered over the diameter of our probe beam. Both sensitivity and specificity (Table 2) are measures that describe the accuracy with which one tissue type is represented by a single cluster. Sensitivity is the probability for all measurements of one tissue type to be grouped into the same cluster. Specificity is the probability that all measurements grouped into the same cluster belong to the same tissue type. For skin, the specificity for cluster B is 69%, which is surprisingly high. The sensitivities obtained show that longitudinally oriented striated muscle and skin separate from the randomly oriented samples almost completely by azimuthal scattering. The *a posteriori* sensitivity and specificity of clustering is impressive considering the limited data used for the analysis. To emphasize the importance of $I(\varphi)$, we have neglected all other information. Our statistical analysis of the azimuthal angle of SLS experiments on supercellular but not macroscopic length scales shows the influence of structure and order in light scattering from thin-tissue sections.

4. Discussion

We have measured SLS patterns from small illumination volumes in thinly cryosectioned tissue in order to understand the origin of light–tissue interactions. First, we reproduced previous results on average scattering form factors. Then we reviewed the motivation for considering organization to be a significant component of the light–tissue interaction. First, the influence of structure can be seen in the large-angle power-law decay of the tissue form factor. Second, the complex azimuthal dependence of the scattering patterns is a consequence of tissue organization.

The common working hypothesis about the origin of light scattering from tissue is that small, mainly spherical objects are responsible for the scattering signal. As a result, many investigations focus on micrometer-sized organelles such as vesicles, mitochondria, and nuclei.[18,22] Our measurements suggest that progress may be enhanced by considering local order within the tissue and the cell. This approach will not have difficulty with tissues consisting mainly of extracellular matrix, such as clots, connective tissues, and dermis. The SLS signal will capture the organizational features of mesh and bundle size, and very likely their disturbance due to disease with higher precision than obtained previously. We have shown that the light-scattering microscope is sensitive to heterogeneities and directionally ordered structure. The relative presence of oriented structure and the relative contribution of heterogeneities to light scattering are optical signatures of the state of the tissue. More-challenging heterogenous tissues whose architecture involves different cell sizes and shapes that form various structural elements become quantifiable, since no prediction about scatterer shape has to be made for data analysis. Our relative success in tissue classification using a small subset of scattering data and fairly primitive analytic methods is intriguing. It suggests a strategy to use differences in light-scattering patterns to distinguish between normal and dysplastic tissue.[18,19,21] The Richards–Kortum group, for example, combines organization and content in a fluorescence-based approach to the optical diagnosis of cervical cancer.[39,40]

The light-scattering microscope can easily be automated to raster scan a sample or region of interest on a sample, which might enable applications in automated quantitative histology. Because routine pathology still requires time-consuming detailed visual inspection of the whole biopsy slice, a major advance might consist of a fast automated raster inspection using a combination of both qualitative imaging and quantitative light-scattering analysis to find small suspicious regions worth inspecting in detail.

Our report also suggests that attempts to extend models of light transport in tissue to shorter distances may be hindered by the existence of locally preferred directions for light transport. Modeling the transition from photon diffusion to a few or single scattering events is difficult because the details of tissue organization become significant. The information about the single-scattering event from the light-scattering microscope might provide important input for corrections of diffusion and transport calculations. One application of such knowledge could be for calculations of exposure for photodynamic therapy that take into consideration the shadows and bright spots created by local tissue structures. In summary, researchers in the fields of optical histology and light-transport modeling may find the light-scattering microscope to be a valuable tool.

We gratefully acknowledge the generous gift of excised frozen *Rana bifida* Sartorius muscle from Pierre Tijskens (University of Pennsylvania). Furthermore, we thank David Boas (Massachusetts General Hospital) for the porcine samples, Jia Quian Ren (Massachusetts General Hospital) for the opportunity to use the cryomicrotome in his institute, and Marge Lehman (Unilever Research) for preparing preliminary samples. This study was supported in part by Unilever Research.

References

1. G. J. Tearney, M. E. Brezinski, B. E. Bouma, S. A. Boppard, C. Pitris, J. F. Southern, and J. G. Fujimoto, “*In vivo* endoscopic biopsy with optical coherence tomography,” Science **276,** 2037–2039 (1997).
2. A. M. Siegel, J. J. A. Marotas, and D. A. Boas, “Design and evaluation of a continuous-wave diffuse optical tomography system,” Opt. Express **4,** 287–298 (1999), http://www.optics-express.org.
3. S. J. Matcher, “Nonuniqueness in optical tomography: relevance of the P1 approximation,” Opt. Lett. **24,** 1729–1731 (1999).

4. J. M. Schmitt and G. Kumar, "Optical scattering properties of soft tissue: a discrete particle model," Appl. Opt. **37,** 2788–2797 (1998).
5. G. Videen and D. Ngo, "Light scattering multipole solution for a cell," J. Biomed. Opt. **3,** 212–220 (1998).
6. B. Chance, N. G. Wang, M. Maris, S. Nioka, and S. Sevick, "Quantification of tissue optical characteristics and hemoglobin desaturation by time- and frequency-resolved multi-wavelength spectrophotometry," Adv. Exp. Med. Biol. **317,** 297–304 (1992).
7. J. B. Fishkin, O. Coquoz, E. R. Anderson, M. Brenner, and B. J. Tromberg, "Frequency-domain photon migration measurements of normal and malignant tissue optical properties in a human subject," Appl. Optics **36,** 10–20 (1997).
8. W.-F. Cheung, S. A. Prahl, and A. J. Welch, "A review of the optical properties of biological tissues," IEEE J. Quantum Electron. **26,** 2166–2185 (1990).
9. F. Bevilacqua, P. Marquet, C. Depreursinge, and E. B. De Haller, "Determination of reduced scattering and absorption coefficients by a single charge-coupled device array. II. Measurements on biological tissue," Opt. Eng. **34,** 2064–2069 (1995).
10. A. H. Hielscher, R. E. Alcouffe, and R. L. Barbour, "Comparison of finite-difference transport and diffusion calculations for photon migration in homogenous and heterogenous tissues," Phys. Med. Biol. **43,** 1285–1302 (1998).
11. D. A. Boas, M. A. O'Leary, B. Chance, and A. G. Yodh, "Scattering of diffuse photon density waves by spherical inhomogeneities within turbid media: analytic solutions and applications," Proc. Natl. Acad. Sci. USA **91,** 4887–4891 (1994).
12. F. Bevilacqua and C. Depreursinge, "Monte Carlo study of diffuse reflectance at source–detector separations close to one transport mean free path," J. Opt. Soc. Am. A **16,** 2935–2945 (1999).
13. V. V. Tuchin, "Light scattering studies of tissues," Phys. Usp. **40,** 494–515 (1997).
14. S. J. Matcher, M. Cope, and D. T. Delpy, "*In vivo* measurements of the wavelength dependence of tissue-scattering coefficients between 760 and 900 nm," Appl. Opt. **36,** 386–396 (1997).
15. S. P. Treweek and J. C. Barbenel, "Direct measurement of the optical properties of breast skin," Med. Biol. Eng. Comp. **34,** 285–289 (1995).
16. D. J. Smithies and P. H. Butler, "Modelling the distribution of laser in port wine stains with the Monte Carlo method," Phys. Med. Biol. **40,** 701–731 (1995).
17. E. Luther and L. A. Kamentsky, "Resolution of mitotic cells using laser scanning cytometry," Cytometry **23,** 272–278 (1996).
18. J. R. Mourant, J. P. Freyer, A. H. Hielscher, A. A. Eick, D. Shen, and T. M. Johnson, "Mechanisms of light scattering from biological cells relevant to noninvasive optical-tissue diagnosis," Appl. Opt. **37,** 3586–3593 (1998).
19. F. Bevilacqua, P. Marquet, O. Coquoz, and C. Depreursinge, "Role of tissue structure in photon migration through breast tissues," Appl. Opt. **36,** 44–51 (1997).
20. S. L. Jacques, C. A. Alter, and S. A. Prahl, "Angular dependence of HeNe laser light scattering by human dermis," Lasers Life Sci. **1,** 309–333 (1987).
21. J. R. Mourant, I. J. Bigio, J. Boyer, R. L. Conn, T. Johnson, and T. Shimada, "Spectroscopic diagnostic of bladder cancer by elastic light scattering," Laser Surg. Med. **17,** 350–357 (1995).
22. L. T. Perelman, V. Backman, M. Wallace, G. Zonios, R. Manoharan, A. Nusrat, S. Shields, M. Seiler, C. Lima, T. Hamano, I. Itzkan, J. VanDam, J. M. Crawford, and M. S. Feld, "Observation of periodic fine structure in reflectance from biological tissue: a new technique for nuclear size distribution," Phys. Rev. Lett. **80,** 627–630 (1998).
23. A. H. Hielscher, J. R. Mourant, and I. J. Bigio, "Influence of particle size and concentration on the diffuse backscattering of polarized light from tissue phantoms and biological cell suspensions," Appl. Opt. **36,** 125–135 (1997).
24. A. H. Hielscher, A. E. Eick, J. R. Mourant, D. Shen, J. P. Freyer, and I. J. Bigio, "Diffuse backscattering Mueller matrices of highly scattering media," Opt. Express **1,** 441–453 (1998), http://www.opticsexpress.org.
25. M. T. Valentine, A. K. Popp, P. D. Kaplan, and D. A. Weitz, "Microscope-based static light scattering apparatus," Opt. Lett. **26,** 890–892 (2001).
26. A. K. Popp, M. T. Valentine, P. D. Kaplan, and D. A. Weitz, "Light scattering microscope to investigate heterogeneities of tissues," in *Optical Biopsy III*, R. R. Alfano, ed., Proc. SPIE **3917,** 22–33 (2000).
27. P. D. Kaplan, V. Trappe, and D. A. Weitz, "Light scattering microscope," Appl. Opt. **38,** 4151–4157 (1999).
28. L. G. Henyey and J. L. Greenstein, "Diffuse radiation in the galaxy," Astrophys. J. **93,** 70–83 (1941).
29. S. T. Flock, B. C. Wilson, and M. S. Patterson, "Total attenuation coefficients and scattering phase functions of tissues and phantom materials at 633 nm," Med. Phys. **14,** 835–841 (1987).
30. R. Marchesini, A. Bertoni, S. Andreola, E. Melloin, and A. E. Sichirollo, "Extinction and absorption coefficients and scattering phase functions of human tissues *in vitro*," Appl. Opt. **28,** 2318–2324 (1989).
31. P. Dimon, S. K. Sinha, D. A. Weitz, C. R. Safinya, G. S. Smith, W. A. Varady, and H. M. Lindsay, "Structure of aggregated gold colloids," Phys. Rev. Lett. **57,** 595–598 (1986).
32. T. Nicolai, D. Durand, and J.-C. Gimel, "Scattering properties and modelling of aggregating and gelling systems," in *Lightscattering: Principles and Development*, W. Brown, ed. (Oxford University Press, New York, 1996).
33. M. Takeda, T. Norisuye, and M. Shibayama, "Critical dynamics of cross-linked polymer chains near the gelation threshold," Macromol. **33,** 2909–2915 (2000).
34. J. Teixeira, "Experimental methods for studying fractal aggregates," in *On Growth and Form*, H. E. Stanley and N. Ostrowski, eds. (Martinus Nijhoff, Dordrecht, The Netherlands, 1986), pp. 145–162.
35. B. Mandelbrot, *The Fractal Geometry of Nature* (Freeman, New York, 1982).
36. J. M. Schmitt and G. Kumar, "Turbulent nature of refractive-index variations in biological tissue," Opt. Lett. **21,** 1310–1312 (1996).
37. R. K. K. Wang, "Modelling optical properties of soft tissue by fractal distribution of scatterers," J. Mod. Opt. **47,** 103–120 (2000).
38. H. C. van de Hulst, *Lightscattering by Small Particles* (Dover, New York, 1981).
39. W. S. Bickel and W. M. Bailey, "Stokes vectors, Mueller matrices and polarized light," Am. J. Phys. **53,** 468–478 (1985).
40. H. Liu, D A Boas, Y. Zhang, A. G. Yodh, and B. Chance, "Determination of optical properties and blood oxygenation in tissue using continuous NIR light," Phys. Med. Biol. **40,** 1983–1993 (1995).
41. N. Ramanujam, M. Follen Mitchell, A. Mahadevan-Janson, S. L. Thomsen, G. Staerkel, A. Malpica, T. Wright, N. Atkinson, and R. Richards-Kortum, "Cervical cancer detection using a multivariate statistical algorithm based on laser-induced fluorescence spectra at multiple wave lengths," Photchem. Photobiol. **64,** 720–735 (1996).
42. N. Ramanujam, M. Follen Mitchell, A. Mahadevan, S. Thomsen, G. Staerkel, A. Malpica, T. Wright, N. Atkinson, and R. Richards-Kortum, "Development of a multivariate statistical algorithm to analyze human cervical tissue fluorescence spectra acquired *in vivo*," Lasers Surg. Med. **19,** 46–62 (1996).